Research papers

Hydrologic connectivity and dynamics of solute transport in a mountain stream: Insights from a long-term tracer test and multiscale transport modeling informed by machine learning

Phong V.V. Le [a,*], Saubhagya S. Rathore [a], Ethan T. Coon [a], Adam Ward [b], Roy Haggerty [c], Scott L. Painter [a,*]

[a] *Environmental Sciences Division and Climate Change Science Institute, Oak Ridge National Laboratory, Oak Ridge, TN, USA*
[b] *Department of Biological and Ecological Engineering, Oregon State University, Corvallis, OR, USA*
[c] *Department of Geology and Geophysics, Louisiana State University, Barton Rouge, LA, USA*

ABSTRACT

The movement of solutes in a watershed is a complex process with multiple interactions and feedbacks across spatial and temporal scales. Modeling the dynamics of solute transport along diverse hydrologic pathways within watersheds – from hillslopes to stream channels and in and out of the hyporheic zones – is challenging but critically important, as these processes integrate and contribute to the biogeochemical functioning of the river corridor up to the river network scale. Here we use results from a long-term network-scale tracer test at the H.J. Andrews experimental forest in western Cascade Mountains, Oregon, USA to inform a multiscale framework for transport in stream corridors. The framework uses a Lagrangian-based subgrid model to represent the effects of hyporheic exchange flow and advective transport at stream network scales. The spatially and temporally resolved stream discharge needed for the transport model is imputed across the river system by an entity-aware long short-term memory network. Modeled concentrations show good agreements with the observations and exhibit power scaling laws indicative of a very wide range of timescales over which hyporheic exchange flow occurs. Our results demonstrate a data-informed modeling framework that links dynamical processes occurring at small scales to a network context to help understand how changes at reach scale cascade into network-scale effects, providing a useful tool for sustainable river basin management.

1. Introduction

Over the past few decades, there has been growing interest in understanding the complex processes in the hyporheic zone (HZ) - regions of sediment below and surrounding the channel that are permeated with stream water (Cardenas, 2015). Much attention has been paid to the physics, biogeochemistry, and ecology of hyporheic exchange flow (HEF) (Boulton et al., 1998; Boano et al., 2014; Ward, 2016). In fact, the exchange of water between stream and the HZ has been recognized as an important process of the stream ecosystems and underpins a host of water quality benefits along river corridors (Harvey and Fuller, 1998; Packman and Brooks, 2001). This process is generally characterized by bidirectional transport of mass (e.g., water and solutes), energy (e.g., heat), and living organisms (e.g., bacteria) between the stream channel and HZ (Tonina and Buffington, 2011; Gomez et al., 2012; Gomez-Velez et al., 2014) and has been found to control biogeochemical cycling and ecological functioning over larger spatial scales (Fuller

and Harvey, 2000; Conant et al., 2004; Battin et al., 2008; Mulholland et al., 2008; Runkel, 2007; Palumbo-Roe et al., 2012; Schaper et al., 2018).

Modeling solute transport in river networks, including the effects of HEF, is critical to evaluating environmental response of a basin – defined as the time varying quantities of interest (e.g., nutrients, contaminants) at the basin outlet – to natural and anthropogenic disturbances. Because watersheds contain networks of dynamically connected paths, this response is largely controlled by the river network geometry through time delays and transformations imposed by the physics of the environmental process operating on the network (Riml and Wörman, 2011; Ye et al., 2012; Czuba and Foufoula-Georgiou, 2014). Therefore, a fundamental but challenging problem is how to integrate transport mechanisms across a wide range of scales to understand the process of water flow and solute transport through a network of diverse hydrologic pathways, including hillslopes, stream reaches, HZs, etc. (Gooseff

---

* Corresponding authors.
E-mail addresses: lepv@ornl.gov (P.V.V. Le), paintersl@ornl.gov (S.L. Painter).

et al., 2008; Rodriguez-Iturbe et al., 2009; Boano et al., 2014; Bertuzzo et al., 2017).

Several modeling approaches have been developed to advance our understanding of HEF and biogeochemical processing in the HZ. For instance, high-dimensional and physics-based transport models have long been used to describe pore water flows and associated HEF (Packman and Brooks, 2001; Revelli et al., 2008; Cardenas, 2009; Boano et al., 2009, 2010; Marzadri et al., 2012; Azizian et al., 2017; Dwivedi et al., 2018). However, since biogeochemical conditions can vary rapidly over very short distances in the HZ and this variability is an important determinant of the overall function (Hedin et al., 1998), these models often require computational meshes with very fine spatial resolution and therefore are only tractable at relatively small spatial scales (e.g., a single morphological feature with explicit representation of streambed topography). At reach scales, a common strategy is to use a transient storage model (TSM), which conceptualizes a finite-size, well-mixed transient storage zone (TSZ) coupled to the main channel by first-order mass exchange (Bencala and Walters, 1983; Runkel and Chapra, 1993; Harvey et al., 1996; Runkel, 1998). The TSM temporarily holds solute and delays downstream transport for time scales longer than advection and dispersion (Bencala et al., 2011). However, the TSMs enforce an exponential distribution of residence times in the HZ, which is inadequate to capture a long tail of solute residence times that can be biogeochemical important by providing sufficient time to experience anoxic conditions and thus affect biogeochemical function (Zarnetske et al., 2011). To better represent the wide-ranging residence times of solute arrivals, alternative parameterizations have been proposed with different mathematical exchange characterizations between the main channel and TSZs, including the continuous time random walk (Boano et al., 2007, CTRW), multirate extensions to the TSM (Fang et al., 2020), and integrodifferential approaches using lognormal (Wörman et al., 2002), power law (Haggerty et al., 2002; Gooseff et al., 2003), and shape-free (Liao and Cirpka, 2011; Liao et al., 2013; Knapp and Cirpka, 2017) travel time distributions.

Network-based models for reactive transport at watershed and river-basin scales have long been developed (Whitehead et al., 1998; Mulholland et al., 2008; Bertuzzo et al., 2017; Czuba et al., 2018). Nevertheless, the majority of network-based models do not explicitly account for mass transfer limitations between the flowing stream channel and biogeochemically active HZs. Without explicit separation of in-channel and out-of-channel processes, reaction rates become effective rates that incorporate the effects of biogeochemical processes, mass transfer limitations, and advective delays and flowpath diversity in the HZ (Jan et al., 2021). As a result, the link to laboratory and site-scale investigations of biogeochemical processes is tenuous at best. Among advancements needed for modeling biogeochemical dynamics at river network scales, Helton et al. (2011) highlighted improvements in the representation of hydrologic exchanges between the stream channel and subsurface waters coupled to more mechanistic representations of biogeochemical cycles.

Motivated by stochastic Lagrangian approaches (Dagan and Cvetkovic, 1993; Cvetkovic and Dagan, 1994; Marzadri et al., 2011, 2012, 2013; Azizian et al., 2015; Sanz-Prat et al., 2015) for efficiently representing a diversity of groundwater flowpaths, Painter (2018) developed a multiscale framework (Advection Dispersion Equation with Lagrangian Subgrids – ADELS) that describes the HZ transport system in Lagrangian form as a subgrid model with hyporheic age replacing the spatial coordinate. In ADELS, each subgrid model represents an ensemble of streamlines that are diverted into the HZ before returning to the channel. The underlying principle is that all HZ streamlines originating from a given channel grid cell have the same upstream boundary condition governed by the concentration in the stream channel; thus the concentration as a function of hyporheic age is identical along the streamlines, differing only by the time required to return to the stream channel, the hyporheic lifetime or travel time. This means that only a single representative pathway needs to be simulated for each channel grid cell and the ensemble result can be recovered by integrating information at various ages along the subgrid simulation, allowing for relatively coarse discretization of the stream channel network while still capturing the effects of fine-scale geochemical variability within the HZ. In its original form, ADELS was limited to steady-state flow. An extended formulation of ADELS that removes this limitation to account for unsteady flow at reach scales was recently introduced by Le et al. (2023).

In a previous work, Jan et al. (2021) developed a network-based transport model based on the original ADELS formulation to simulate biogeochemical processes at watershed scales. However, this model was limited to steady-state flow in the stream channels using specified mean annual streamflow across the network. Given the dynamic nature of stream and river systems, the steady-state flow restriction clearly limits the usefulness of this model for applications that require longer time frames. In this paper, we extend the ADELS model that removes the steady-discharge constraint as in Le et al. (2023) to represent long-term dynamics of HEF and solute transport at watershed scales. That is, we seek to develop a dynamic connectivity framework for capturing the complexity of multiscale transport on a network and then evaluate it against a season-long tracer test. Watershed-scale transport analyses require a representation of spatio-temporal dynamics of streamflow over the entire watershed including contributions from sub-catchments of various sizes. As an alternative to a calibrated process-based flow model, we reconstruct streamflow over an entire watershed using a rainfall-runoff model based on the entity-aware long short-term memory (EA-LSTM) neural network (Kratzert et al., 2019b) that allows for learning similarity and discrimination between different sub-catchments as a feature in the deep learning framework. We then compare the breakthrough curves (BTCs) simulated using multiscale framework to observed BTCs obtained from multiple locations during a months-long tracer test in a mountain watershed.

2. Methodology

Our approach relies on performing a process-based scaling of the stream network geometry (i.e., width function) to construct a time response function for the process of interest (e.g. solute exports). This scaling involves three main steps: establishing a directed graph representing the stream network (Section 2.1), generating streamflow on the established graph (Section 2.2), and multiscale modeling and tracking of solute transport on the graph (Section 2.3).

2.1. Graph representation of transport in streams

Let the stream network be defined by a root-directed binary spanning tree $T = (V, E)$, consisting of a set of vertices or nodes, $V = \{v_i\}$, and a set of edges or links, $E = \{e_{ij}\} \subseteq \{(v_i, v_j) \mid (v_i, v_j) \in V \times V\}$, $i, j = 1, \ldots, N$, where e_{ij} represents the flow from v_i to v_j and $|V| = N$ is the number of nodes (Fig. 1a). The in-degree k_i^{in} and out-degree k_i^{out} of a node v_i are the number of incoming and outgoing links, respectively. By construction, $k_i^{in} \leq 2 \ \forall \ v_i \in V(T)$ for binary trees. We define a node with $k^{in} = 0$ as a *source*, $k^{in} = 1$ as an *intermediate*, and $k^{in} = 2$ as a *junction*. Source nodes are the points farthest upstream in the network with a drainage area larger than a minimum threshold $A \geq A_{min}$, whereas junctions are the points at which two streams or edges join. To set the maximum length of $e_{ij} \in E(T)$, when the along-stream geographic distance between two nodes forming an edge e_{ij} is greater than a threshold d_{max}, intermediate nodes are added to split the edge e_{ij} into shorter ones. For the purpose of this study, branching of edges is not allowed or equivalent to $k_i^{out} = 1 \ \forall \ v_i \in V(T) \backslash v_1$ (except at the root v_1, which corresponds to the basin outlet where $k_1^{out} = 0$).

For any $v_i \in V(T)$, we can delineate a corresponding sub-basin Ω_i, which can be represented by a tree T_i. It is easy to see that T_i is a subtree of T "rooted" at v_i. We can also assign to each v_i a set of hydrological attributes ζ_i of the sub-basin Ω_i such as the upstream
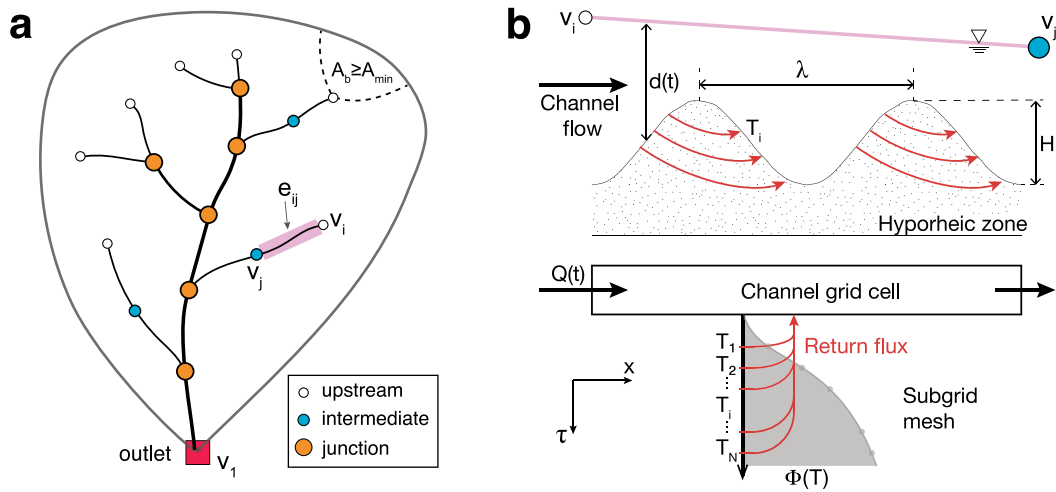
Fig. 1. Conceptual graph-based framework of a multiscale representation of transport in a river network under unsteady flow. (a) Illustration of a watershed with channel network characterized by edges and different types of vertices. The highlighted segment of the network is an edge e_{ij} connecting nodes v_i and v_j. (b) Schematic of ADELS in edge e_{ij} under unsteady flow conditions. Hyporheic zone (HZ) transport is represented by subgrid models in residence time τ formulation, which are coupled to the stream channel. The subgrid auxiliary equation associated with each channel grid cell is representative of the ensemble of pathways (red arrows) within the grid cell. Gray shading illustrates the cumulative travel time distribution of hyporheic lifetime. (For interpretation of the references to color in this figure legend, the reader is referred to the web version of this article.)
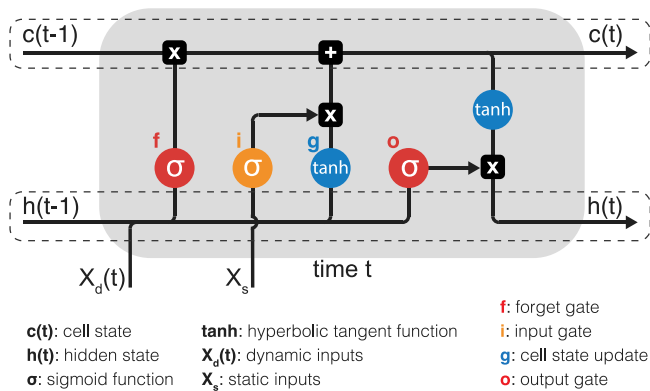

Fig. 2. Schematic diagram of the Entity-Aware-LSTM neural network. The cell states $\mathbf{c}(t)$ characterizes the memory of the system. Dynamic inputs $X_d(t)$ (e.g., precipitation, temperature) are passed in the forget gate $\mathbf{f}$, whereas static inputs X_s (e.g., catchment attributes) are processed through the input gate $\mathbf{i}$.

drainage area A_Ω [L^2], average slope $\bar{s}_\Omega$ [–], average aspect $\bar{a}_\Omega$ [rad], average elevation $\bar{z}_\Omega$ [L], length ℓ_Ω [L], and perimeter p_Ω [L] of the sub-basin Ω_i. These attributes ζ_i are assumed to be constant over time. To each edge $e_{ij} \in E(T)$ we assign a state ξ_{ij} which includes hydraulic conditions of the corresponding stream segment such as the average streamflow Q_{ij} [L^3 T^{-1}], average wet cross-section area A_{ij} [L^2], cross-section average depth d_{ij} [L], and cross-section average width w_{ij} [L], etc. While not indicated explicitly, the attributes of ξ_{ij} may be a function of time to capture possible time-varying properties of the system. Here we use hydraulic geometry scaling (Leopold and Maddock, 1953) to relate time-dependent width, depth, and thus cross-section area to time-dependent Q_{ij}. Hydraulic geometry scaling provides general trends of those quantities albeit with significant uncertainty. Stream-specific relationships can be used instead when that information is available from detailed field investigations.

2.2. Deep learning rainfall-runoff reconstruction of streamflow

We next develop a rainfall-runoff model based on the EA-LSTM neural network (Kratzert et al., 2019b) to reconstruct streamflow for all sub-basins Ω_i for $i = 1, \ldots, N$. An overview of the EA-LSTM network is given in Appendix A. The LSTM-based networks can generalize to

ungauged basins with better overall skill than calibrated conceptual models in gauged basins (Kratzert et al., 2019a). Here, each sub-basin Ω_i has a unique set of static hydrological attributes ζ_i and its outlet corresponds to the node $v_i \in V(T)$. Unlike the standard LSTM network (Hochreiter and Schmidhuber, 1997), the EA-LSTM considers both static and dynamics inputs; and it conditions the processing of the latter on a set of the former (Fig. 2). This design enables the EA-LSTM network to simultaneously learn from both the time-independent catchment characteristics (e.g., geometry, slope, etc.) and long-term dependencies (e.g., precipitation and subsurface water storages). In particular, it explicitly differentiates between similar types of dynamical behaviors (here rainfall-runoff processes) that differ between individual entities (here sub-basins) and provide a universal set of model parameters for all the sub-basins Ω_i. This universality is useful for modeling streamflow from precipitation for multiple sub-catchments within a single river basin.

An objective function is required to train the EA-LSTM network. Since model training is across multiple sub-basins, a function that does not depend on the basin-specific outputs is required to avoid bias. Here, the basin-averaged Nash–SutcliffeEfficiency (NSE) index (Kratzert et al., 2019b, see Appendix A) is used as a loss function for training in the EA-LSTM. To avoid overfitting and select the most significant static inputs, we examine different subsets of catchment attributes selected from ζ_i. For each subset, the EA-LSTM network is trained and evaluated with the same dynamics inputs (e.g., meteorological forcing). The subset that shows the best performance during evaluation period (highest median NSE) is chosen as the catchment attributes for the ML-based rainfall-runoff model to generate streamflow used for solute transport modeling. Similar to standard LSTM model, the EA-LSTM is not based on physical principles and thus does not guarantee mass conservation. However, Frame et al. (2022) showed that the mass-conserving LSTM (Hoedt et al., 2021, MC-LSTM) did not perform as well as the standard (non-physical) LSTM at simulating peak flows and out-of-sample events.

2.3. Multiscale model of transport in stream network

We use the recently introduced unsteady ADELS framework (Le et al., 2023) to simulate solute transport in the stream network (i.e., on the directed binary tree graph T), including processes in the stream channels and the associated HZs (Fig. 1b). The ADELS model describes the HZ transport system in Lagrangian form as a 1-D vertical subgrid
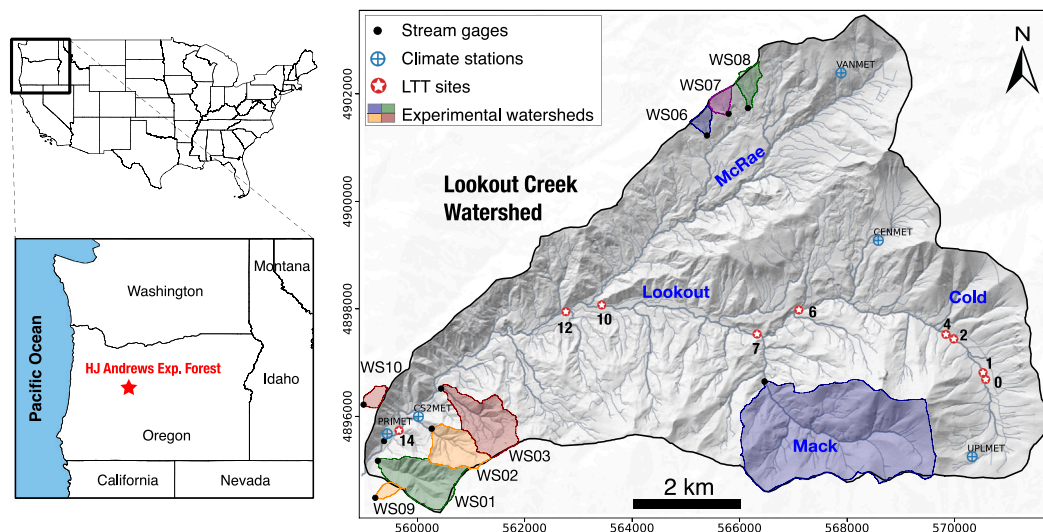
Fig. 3. Map of the H.J. Andrews Experimental Forest, Blue River, Oregon, showing main tributaries, experimental watersheds, stream gage locations, weather stations, and the longitudinal tracer test (LTT) sites.

model. The subgrid model for each channel grid cell represents the ensemble of streamlines diverted into the HZ by all subgrid hydrogeomorphic features, such as bedforms, meander bends, alternating point bars, and pool-riffle complexes. That is, the model is an upscaled representation with an implied scale for the channel representation (Painter, 2018). The detailed formulation of ADELS framework with unsteady flow is presented in Le et al. (2023) and summarized in Appendix B.

The unsteady ADELS framework has been implemented in the multiphysics Amanzi-ATS model (Coon et al., 2019). Here we apply this framework on the directed graph T under the proportionality and superposition assumption of linear system theory for multiscale modeling solute transport at the watershed scale. Specifically, for all edges $e_{ij} \in$ E(T), topologically defined meshes are created within each edge to prescribe the discrete representation of the domain (i.e., grid cells) on which Eq. (B.1) are solved. Mass balance constraints are imposed at intermediate and junction nodes to link river segments, and Amanzi-ATS solves the transport equation over the entire network as a linear system. Topological mesh allows both stream networks (1D submanifolds whose coordinate is defined as distance along the network) and the subgrid mesh (1D submanifold whose coordinate is in travel time) to be coupled in the existing mesh infrastructure of Amanzi-ATS (Jan et al., 2021). Geochemical reactions (e.g. sorption) are implemented in the open-source PFLOTRAN (Hammond et al., 2014) called in Amanzi-ATS through the programming interface Alquimia (Andre et al., 2013; Molins et al., 2022). Here the time series of streamflow is first reconstructed at every node $v_i \in$ V(T) using a rainfall-runoff model based on the EA-LSTM neural network. Next, streamflow in all topological grid cells along an arbitrary edge $e_{ij} \in$ E(T) is linearly interpolated between nodes v_i and v_j for every time step. We note that at junction nodes, the linear interpolation is done before the two upstream reaches join to ensure mass conservation. Then interpolated streamflow along all the edges is used for simulating solute transport described in Eq. (B.1).

3. Application to the H.J. Andrews experimental forest

3.1. Data and site description

We use observational datasets collected in the H.J. Andrews experimental forest (hereafter referred to as HJA) to evaluate the connectivity-based multiscale transport model. The HJA is located in the central Cascade Mountains of Oregon, USA (44.23°N, 122.17°W) and comprises of the entire drainage basin of the Lookout Creek (see Fig. 3). The landscape in the HJA is generally mountainous terrain with

stream erosion, landslides, and past glaciations influencing the stream geomorphology (Swanson, 1975). The climate regime of the HJA is Mediterranean and includes a wet and mild winter and dry and cool summer. The long-term mean annual precipitation ranges from 2200 to 3000 (mm), with about 75% of precipitation occurs during the wet season from November to April (Johnson et al., 2021). The Lookout Creek is a fifth-order watershed and has four tributaries: Cold, Lookout, Mack, and McRae. This watershed is underlain by multiple rock types of volcanic origin Swanson (2005), leading to substantial heterogeneity in baseflow sources within the watershed (Segura et al., 2019).

The tracer data used in this study is obtained from a previous work (Haggerty and Ninnemann, 2013), which consisted of a watershed-wide longitudinal tracer test (LTT) on the main stream of the Lookout Creek (Fig. 3). The LTT was initiated at the beginning of the dry season (June) in summer 2003 and involved an in-stream injection of Rhodamine WT (RWT) at a concentration of 12.5 (g/L) with an average pumping rate of 0.46 (mL/s) over about 77 h at site 0 (Ninnemann, 2005). This continuous injection was followed by a system of monitoring at 8 downstream locations (sites 1, 2, 4, 6, 7, 10, 12, and 14) on the main stream until the end of the dry season (November) in 2003. The monitoring sites were selected at points above and below major confluences, including the Cold Creek, Mack Creek, McRae Creek, as well as a monitoring station at the HJA headquarters near the mouth of Lookout Creek basin. The along-river distance from sites 0 to 14 is approximately 14.27 (km), equivalent to approximately 90% the length of the mainstream Lookout Creek. At each site, concentrations were recorded using a combination of flow-through fluorometers measuring real-time concentrations and grab samples collected with ISCO autosamplers and processed in a laboratory fluorometer (Ninnemann, 2005).

Topographic and long-term hydro-meteorological data are used for developing the rainfall-runoff model. In particular, catchment characteristics are derived from high-resolution (1-m) lidar data and used as the static inputs for the EA-LSTM neural network. Daily precipitation during the period from 1979 to 2020 measured at the Primary Meteorological (PRIMET) station near the downstream of the Lookout Creek (Fig. 3b) is used as the dynamics inputs for the EA-LSTM neural network. Missing data in the PRIMET station is filled by daily precipitation observed at a nearby Climate station (CS2MET) that is also located in the Lookout Creek watershed. Daily streamflow was measured during the same time period (1979–2020) at 9 gaged experimental watersheds in the HJA (including WS01-WS03, WS06-WS10, and Mack Creek) and a United States Geological Survey (USGS) gaging station at the outlet

Table 1

Catchment attributes derived from lidar topographic data for the experimental and Lookout Creek watersheds, including upstream drainage area A_Ω, average slope $\bar{s}_\Omega$, average aspect $\bar{a}_\Omega$, average elevation $\bar{z}_\Omega$, average distance to the sub-basin outlet $\bar{d}_\Omega$, and catchment length ℓ_Ω. Boldface indicates attributes that were selected for the EA-LSTM model to generating streamflow.

Watershed	X [m]	Y [m]	A_Ω [ha]	$\bar{s}_\Omega$ [°]	$\bar{a}_\Omega$ [°]	$\bar{z}_\Omega$ [m]	$\bar{d}_\Omega$ [m]	ℓ_Ω [m]
WS01	559 271	4 895 174	95.57	33.20	204.87	715.16	1 003.3	1,843
WS02	560 273	4 895 771	62.48	31.98	227.83	785.53	633.9	1,239
WS03	560 445	4 896 517	97.44	31.05	220.34	777.49	1,113.2	1,796
WS06	565 394	4 901 228	12.06	16.97	164.46	955.01	318.0	639
WS07	565 796	4 901 632	14.54	18.64	158.19	1015.56	291.0	517
WS08	566 156	4 901 737	20.87	18.12	172.25	1057.77	499.1	901
WS09	559 223	4 894 485	8.63	33.07	243.34	573.53	260.8	554
WS10	559 005	4 896 219	11.82	33.85	246.02	578.67	254.3	498
MACK	566 465	4 896 651	572.87	27.42	194.38	1195.48	2,154.6	4,050
LOOKOUT	559 386	4 895 540	6205.38	24.39	198.70	979.16	10,290.8	17,537

of the Lookout Creek (USGS-14161500). The drainage areas of these 10 watersheds range from 8.5 to 6205 ha (Table 1). Missing streamflow observations were infrequent, except for the WS07, which lacked data between 1988 and 1994. In addition, high-frequency streamflow data were also collected on the main channel of the Lookout Creek at the same 8 monitoring sites and during the same time that the LTT was measured (i.e., dry season 2003). However, the length of these high-frequency streamflow observations varied substantially across the sites and were often very limited. The catchment attributes of the experimental and Lookout Creek watersheds are presented in Table 1.

To put more weight on analyses during the dry season when the LTT was implemented, observed daily streamflow is normalized by the catchment area and then transformed into log space for training the EA-LSTM neural network. This transformation reduces the influence of large streamflow during rainy, wet seasons on the loss function while training the model over a long time period. In this study, the EA-LSTM model training is performed using data from the time period 1 October 1979 through 30 September 2010. The EA-LSTM model testing is done using data from the time period 1 October 2010 through 30 September 2020. The training and testing are applied for all 10 watersheds to obtain a single set of parameters. Next, this parameter set is used to generate streamflow over the entire Lookout Creek watershed (i.e., at each sub-basins Ω_i) for the dry season in 2003 when the LTT was conducted. The hyper-parameters of the EA-LSTM model are set as follows: the number of hidden/cell states is 512, the dropout rate is 0.4, the length of the input sequence is 730, and the number of stacked LSTM layers is 1. For the entire HJA, the catchment attributes selected for the static inputs in the EA-LSTM network to generate streamflow include the mean aspect $\bar{a}_\Omega$, mean elevation $\bar{z}_\Omega$, and length of the sub-basins ℓ_Ω that show the highest value of the median NSE for all sub-basins. The generated streamflow is then used as inputs for the unsteady ADELS multiscale transport model.

The sorption coefficient of RWT solute (K_d) is assumed homogeneous over the river network and selected at half of the value reported in Gooseff et al. (2005) for a headwater sub-catchment (i.e., WS03) within the HJA. This simple adjustment is made because the aforementioned study focused on the fine fraction of the hyporheic sediment sample acquired, and it is likely an overestimate of the true in situ isotherm for hyporheic sediments in the streambed. While this is a strong assumption — which is not necessarily accurate in real-world river networks exhibiting heterogeneities, we find it more plausible than using the reported value, as it offers a conservative approach to mitigate the risk of overestimating the true parameter. It is worth noting that this assumption reduces hyporheic RWT sorption, thus potentially affecting parameters related to the residence time of RWT in the subgrid models. The other solute transport parameters of the ADELS included the travel time distribution $\mathcal{T}$, mean turnover rate α_0, scaling exponent β_α, mean longitudinal dispersion coefficient D_0, and its scaling factor β_D (See Table 2). The Markov chain Monte Carlo (MCMC) optimization method has been employed for parameter estimation in ADELS models at the reach scale (Rathore et al., 2021; Le et al., 2023; Rathore et al., 2023). However, the scalability of the

MCMC approach is challenging as the dimensionality of the problem increases at larger scales. For the sake of simplicity and to concentrate on the network-scale development, model parameters are manually calibrated to minimize the L2 distance between modeled results and observations across all monitoring sites (baseline simulation). It should also be noted that while manual calibration facilitates direct adjustment of parameters to demonstrate the workflow, this approach is less reliable than the MCMC and lacks insight on parameter uncertainty.

To evaluate the impacts of streamflow variation and the HZ on the dynamics of solute transport in the HJA, we compare the baseline simulation against four variant configurations. These four sensitivity experiments purely represent different aspects of the physics modeled in the ADELS framework. The first experiment (E1) excludes the HZ, indicating that solute transport occurs solely in the stream channel. The second experiment (E2) assumes that streamflow remains in a steady-state condition, but with spatial heterogeneity. In the third experiment (E3), variations in streamflow do not affect the mass exchange rate between the channel and HZ, denoted by $\alpha(x,t) = \alpha_0$ in Eq. (B.2). Finally, the fourth experiment (E4) assumes that the speed at which solutes move along streamlines within the HZ is not affected by the variation of streamflow in the channel, i.e., $\nu(x,t) = 1$ in Eq. (B.5). Model parameters other than those specific to each experiment are held the same as in the baseline simulation.

3.2. Network extraction

The stream network of the Lookout Creek watershed in the HJA is extracted from lidar topographic data as shown in Fig. 4. The network includes 22 intermediate and 37 junction nodes (represented by blue and orange circles, respectively) in the stream channels and 38 upstream nodes (represented by open circles) in the upstream of the watershed. The elevation at the upstream and downstream ends of each edge (or stream segment) is extracted from the underlying topography, differenced, and divided by the geographical distance between two corresponding nodes to determine the slope s_{ij} of the edge (indicated by the colorbar). The slope of the water surface is assumed to be equivalent to the slope of the streambed under uniform flow conditions which is likely approximate for most of the stream networks. The heterogeneity of channel slopes within the Lookout Creek watershed, indicated by continuous changes of the slopes from the upstream (more steep) to the downstream (less steep), is likely to lead to non-uniform velocities and magnitude of streamflow along the channels. This suggests the need for including spatially explicit analysis of streamflow variability into solute transport modeling at watershed scales. To simulate transport within the stream channels of the HJA, we discretize the river network domain into computational grid cells with a size of $\Delta x \approx 100$ m. Within each grid cell, a subgrid mesh consisting of 10 cells, characterized by travel time coordinates, is used to capture the fine-scale variability of transport within the HZ. We utilize an explicit upwind numerical scheme for the advection terms in ADELS. This choice is made to preserve positivity and ensure smooth solutions.

Table 2
Parameters used for ADELS model.

Symbol	Description	Unit	Value
K_d	Sorption coefficient	L/g	0.016
α_0	Pseudo-mean rate of water turnover	1/s	4.5×10^{-5}
β_α	Scaling exponent of hyporheic exchange	–	0.09
β_v	Scaling exponent for velocity changes in the HZ	–	0.10
D_0	Mean longitudinal dispersion coefficient	m^2/s	0.011
β_D	Factor representing the fluctuation of dispersion coefficient	–	2.14
$\mathcal{T}_{50}$	50th percentile of the travel time in the HZ	h	2.5
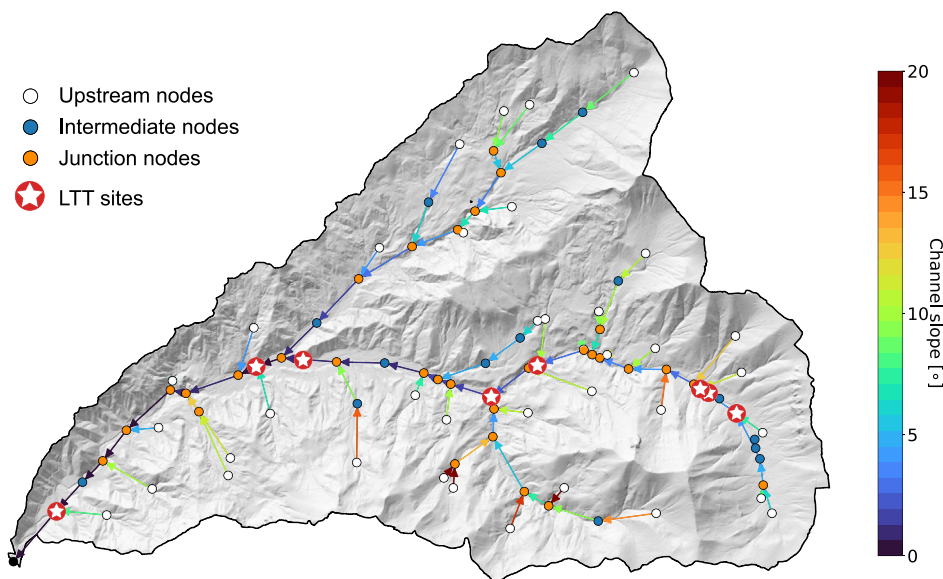
Fig. 4. Graph network of the Lookout Creek watershed in the H.J. Andrews Experimental Forest represented by a spanning binary tree. Small circles denote three different types of nodes; red circles with a star indicate the locations of longitudinal tracer test (LTT) sites. Colorbar indicates the slope of the river segments and arrows represent flow direction. The network is derived from 1-m topographic Lidar data. (For interpretation of the references to color in this figure legend, the reader is referred to the web version of this article.)

Therefore, a stable time step Δt is determined for each iteration based on the CFL condition (Courant et al., 1967).

The relationships between catchment area A_Ω and the mainstream length ℓ_Ω for the 9 experimental and Lookout Creek watersheds are shown in Fig. 5a. Although watershed shape and size vary significantly, this relationship shows a structural relation $\ell_\Omega \approx 2.18 A_\Omega^{0.54}$ and is consistent with commonly reported parameters proposed by Hack (1957) and Montgomery and Dietrich (1992). While this pattern may not be a strict power law in the purest form ($\ell_\Omega \propto A_\Omega^p$), it exhibits power law-like behavior over a wide range of scales with the length of rivers generally increasing sub-linearly with the area of their drainage basins. Here the size of the circles indicates the Gravelius compactness (GC) coeffcient (Gravelius, 1914), a metric of catchment shape defined as the ratio between catchment perimeter and area. The GC values reveal that basin elongation (large GC) does not correlate with a change in the catchment area or size. Moreover, the GC does not correlate with the orientation or aspect of the watershed.

The relationship between ℓ_Ω and A_Ω for all sub-catchments (97 in total) delineated within the Lookout Creek watershed is shown in Fig. 5b. Since the minimum threshold of the upstream nodes used to delineate these sub-catchments is 50 ha, no sub-catchment whose area smaller than this threshold is observed. Similar to the experimental watersheds, the area-length relationship found in all sub-catchments also exhibits the power law-like scaling ($\ell_\Omega \approx 2.25 A_\Omega^{0.5}$) as reported in previous studies (Hack, 1957; Montgomery and Dietrich, 1992). Moreover, the delineated sub-catchments are distributed relatively uniform over a wide range of sizes with GC ranging from 1.45 to 3.49.

3.3. Rainfall runoff modeling

Fig. 6 shows the comparison of normalized daily streamflow obtained from the EA-LSTM model (dashed lines) and observations (solid lines) for the 9 experimental and Lookout Creek watersheds during the testing period (2010–2020). Overall, the fit between observed and modeled daily streamflow is very good quantified by the high values of the NSE index (Nash and Sutcliffe, 1970). Although the size of the experimental watersheds varies substantially that may affect the generating mechanism and persistence of flow on the watersheds, simulated streamflow based on the EA-LSTM neural network is in good agreement with the observations for both dry (low flow) and wet (high flow) seasons. This result demonstrates the ability of the EA-LSTM to construct a universal model that can capture well the dynamics of the rainfall-runoff process not only for Lookout Creek watershed but also for all contributing sub-catchments within the watershed. We note here that the WS07 has about 8 years of missing streamflow data, resulting in lower density of the points in the plot.

Comparison of seasonality in streamflow between observations and EA-LSTM model is further presented in Fig. 7. Overall, the results show that the seasonality is well reproduced in most of the watersheds, except at the WS07 where data are missing for a long period during the model training. This absence of data leads to relatively low NSE values between observations and model for both the dry season and entire year periods. The EA-LSTM slightly overestimates streamflow during the dry season in WS06 and WS09 where the drainage areas are the smallest, resulting in NSE values lower than in other watersheds. Moreover, the results indicate more pronounced seasonality of
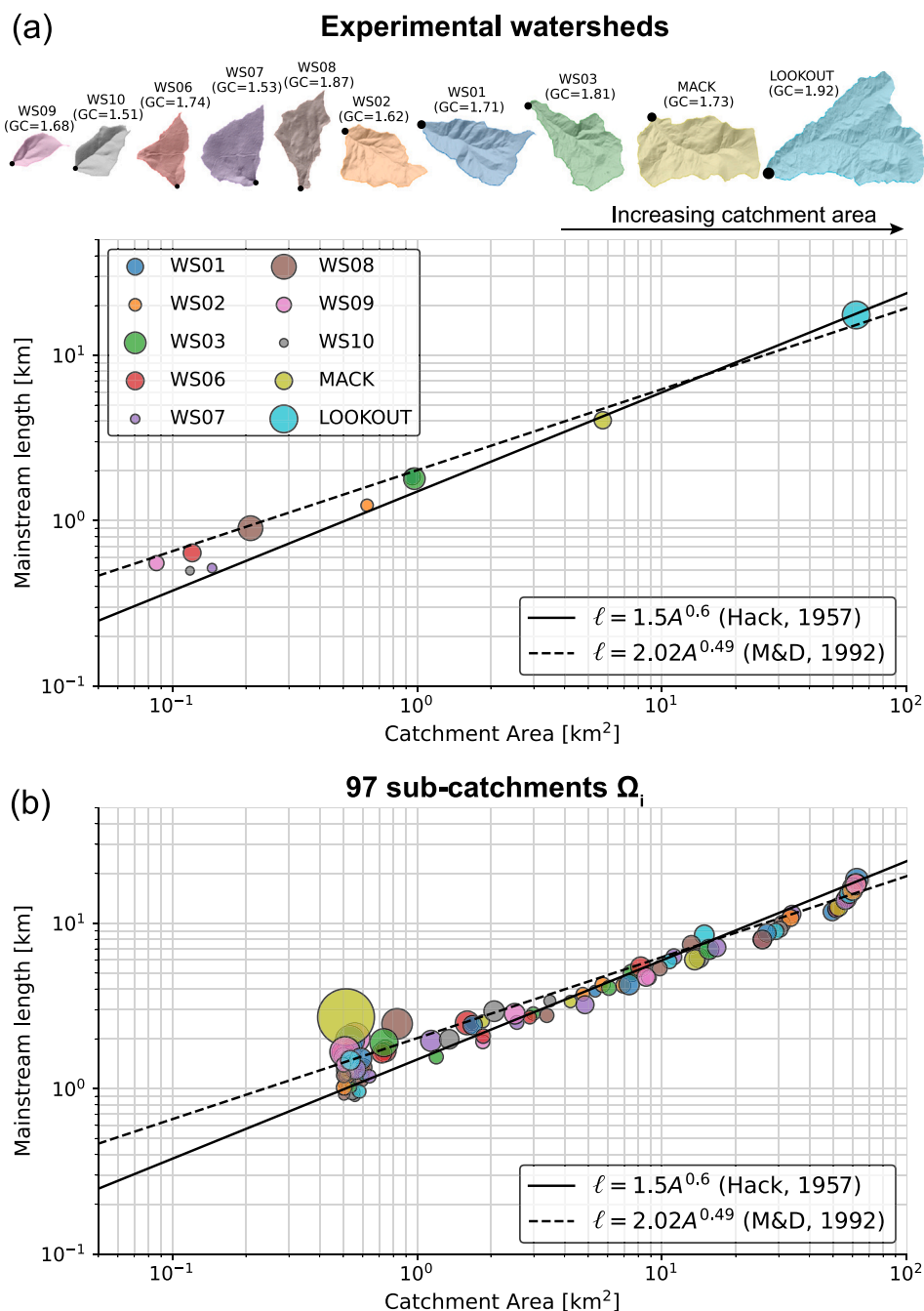
Fig. 5. Relationship between the mainstream length ℓ and catchment area A for (a) 9 experimental and Lookout Creek watersheds and (b) all sub-catchments Ω_i obtained from lidar data within the Lookout Creek watershed. Size of the circle represents the Gravelius coefficients (GC) of the corresponding sub-catchment. Solid and dashed lines show the original Hack's law (Hack, 1957) and the law proposed by Montgomery and Dietrich (1992).

streamflow in the smaller watersheds (e.g., WS06-WS10) compared to the larger ones (e.g., WS02, WS03, Mack, and Lookout), as evidenced by lower magnitudes of streamflow per unit area during dry months. As the normalized streamflow during the wet season exhibits similar magnitudes across all watersheds, the difference in seasonality may be attributed to the effect of groundwater discharge during low flow season, which is often limited in small headwater mountain streams. In fact, the strong seasonality in WS10 (the second smallest watershed) originates from a small fraction of old water that is preferentially released during dry periods (Rodriguez et al., 2018). However, seasonality can also be influenced by additional factors such as climate, landforms, and geology. It is worth noting the contrast in streamflow seasonality between WS01 (strong) and WS03 (weak), despite their

similar sizes. Voltz et al. (2013) suggested that the WS03 valley bottom riparian area is well connected to its stream across a broad range of hydrologic conditions, resulting in weaker seasonality in streamflow compared to WS01. Given that streamflow magnitude significantly impacts transport dynamics, seasonality must be well captured for accurate modeling of solute transport during the dry season.

Streamflow over the entire network is then reconstructed for the dry season (June-November) in 2003 when the LTT was implemented and used for modeling solute transport (see Fig. 8). We note that only site LTT-2 had long observations of streamflow that covered the entire LTT period (~6 months). All other monitoring sites had less than one month of streamflow observations (same length of observations as tracer data). The results show that the EA-LSTM model captures quite well the
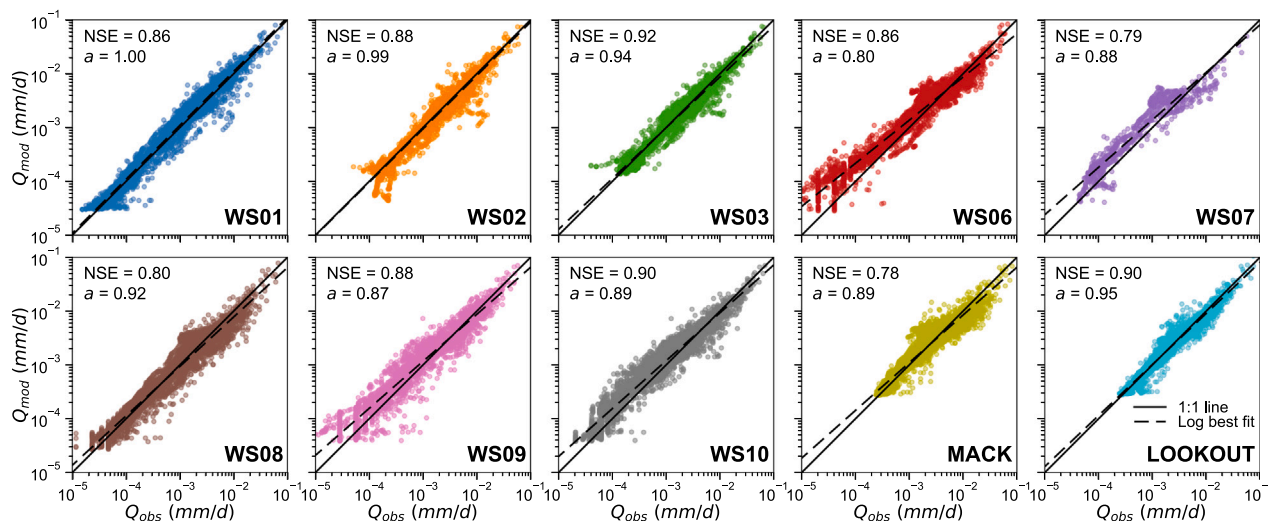
Fig. 6. Comparison of streamflow obtained from EA-LSTM model and observations during the testing period (2012–2021) for 9 experimental and Lookout Creek watersheds. Solid lines show the 1:1 relationship. Dashed lines represent the best fit in log space and *a* indicates the slope of the dashed lines.
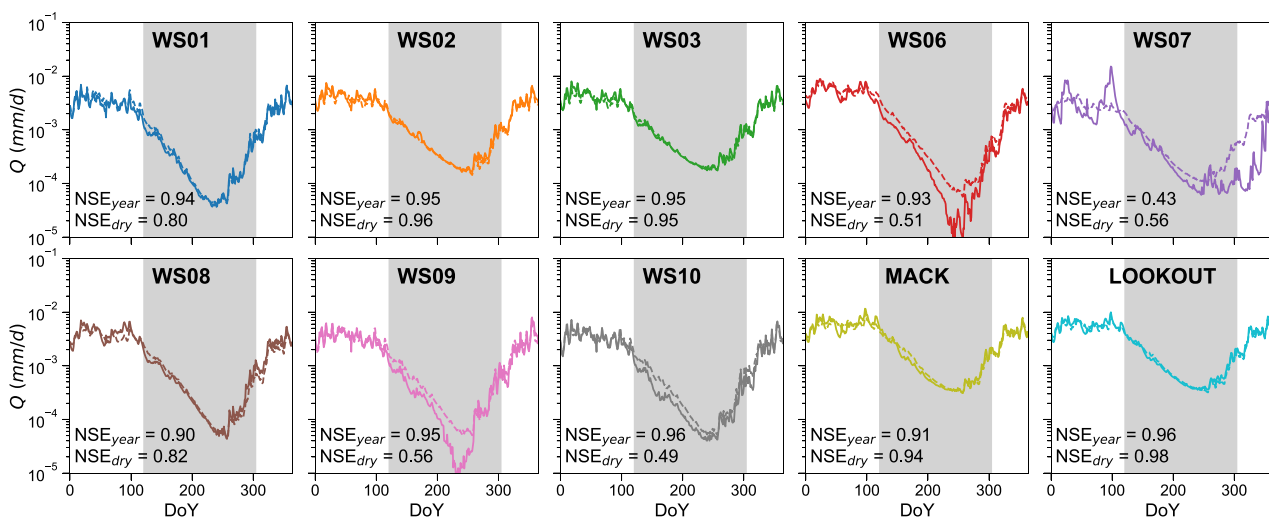

Fig. 7. Comparison of streamflow seasonality between EA-LSTM model (dashed lines) and observations (solid lines) during the testing period (2012–2021) for the 9 experimental and Lookout Creek watersheds. Gray shading indicates dry season. NSE_{year} and NSE_{dry} indicate the NSE values between observations and modeled for entire year and dry season periods, respectively.

magnitudes of streamflow at most of the monitoring sites. However, we observe more variability and steeper slope of modeled streamflow compared to observations in sites LTT-4, LTT-7, and LTT-10. Overall, the results demonstrate that the EA-LSTM model has the potential to reconstruct reasonably well daily streamflow from precipitation data for simulating solute transport at watershed scale during the LTT period.

3.4. Solute transport

Fig. 9a shows the comparison between the observed and modeled BTCs of the RWT tracer for 8 monitoring sites. Three distinct stages are evident in these BTCs. During the initial stage (rising phase), the concentration rises dramatically as the tracer front arrives, especially in the upstream monitoring sites. The model captures well the arrival time of the tracer at most of the monitoring sites, implying that flow velocity along the entire stream network is also well reconstructed. In the second stage, the BTCs become more flat in response to streamflow magnitudes and the topologic structure of the stream network. At the end of the second stage, the BTCs reach the peak values after the

injection ends. However, the time that concentrations reach the peaks also increases along the downstream due to the time delay effect of the geometry of the network. This effect further leads to an increase in the slope of the BTCs at the downstream during this stage. Overall, the good fit between the observations and modeled concentrations at all monitoring sites in the first two stages demonstrates that our model is able to link dynamical processes occurring at small scales into a network context. During the final stage (recession phase), the observed BTCs at all monitoring sites are well approximated by a power law, although the time ranges are somewhat limited. Modeled BTCs are also approximately power-law but with some deviations for LTT-4. Power-law decreases in the BTCs indicate a very wide range of hyporheic residence times (Fig. 9b), as has been noted previously (Haggerty et al., 2002; Gooseff et al., 2003). In other words, the solute and contaminants can remain in the HZ and channel systems for a very long time and this has important implications for stream biogeochemistry and river basin management. Toward the end of the dry season, the modeled BTCs are found to be more variable that could be attributed to the effects of rainfall events in the early wet season (Fig. 9a). However, most of the LTT observations are fairly short, except sites LTT-2 and LTT-4, and
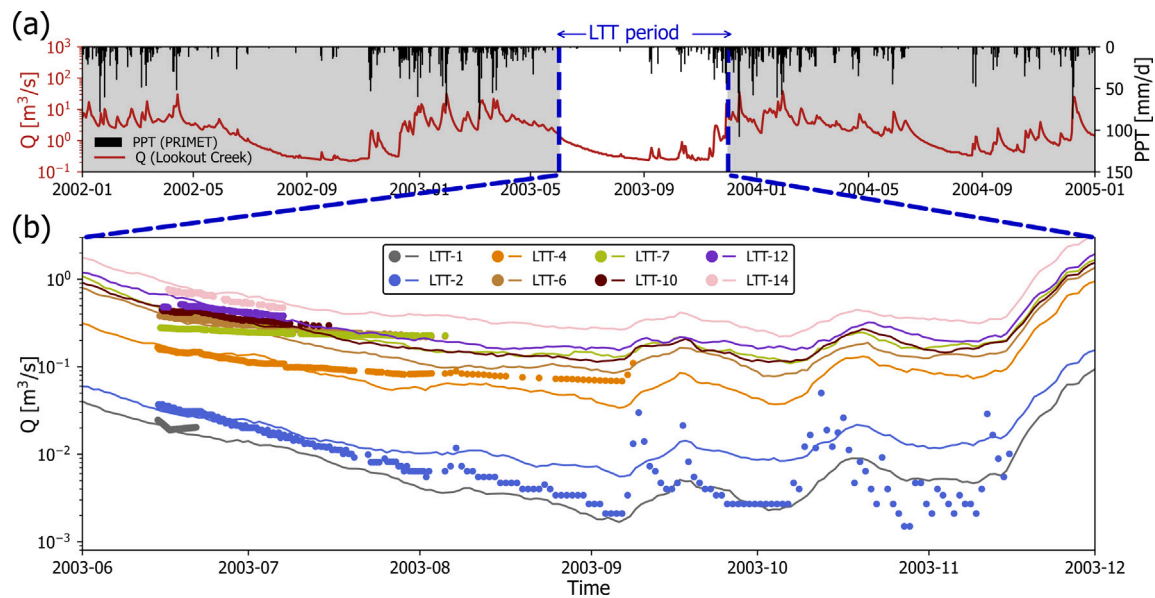
Fig. 8. (a) Time series of observed daily precipitation at PRIMET station (black bars) and streamflow discharge at the outlet of the Lookout Creek (red line) during the period 2002–2004. (b) Comparison of modeled (solid lines) and observed (dots) streamflow at 8 monitoring sites during dry season (June-November) in 2003. Note that the length of streamflow observations varied substantially across monitoring sites and were often very limited. (For interpretation of the references to color in this figure legend, the reader is referred to the web version of this article.)

we are unable to make a comprehensive comparison with the modeled results during this period.

The modeled BTCs obtained from four experiments (E1-E4) are presented in Supplementary Figures S1-S4. In E1, the subgrid is excluded from the channel, resulting in no mass exchange between the stream and HZ. In this case the RWT tracer is swiftly transported out of the river network and the model is unable to capture the long tail distribution of RWT concentration in the system (Figure S1). This is inline with our expectations, and indicates that the representations of the small-scale hyporheic processes are important in modeling the long-term dynamics of solute transport along the river networks. In E2, streamflow is assumed in steady-state condition, and the model fails to capture the arrival time and peaks of concentration of the BTCs at all monitoring sites (Figure S2). This result underscores the crucial role of advection and dilution processes in capturing the complex dynamics of solute transport at the river network scale. In E3, the variations of streamflow do not affect the hyporheic exchange rate α, leading to overestimate of the solute concentration downstream of the river network (Figure S3). This outcome may be attributed to the reduction in solute mass entering the HZ compared to the baseline simulation, resulting in higher RWT concentrations in the stream channel. In E4, streamflow variability had no effect on flow velocity within the HZ, resulting in similar patterns of the BTCs with slightly higher concentration of RWT downstream the river network as in E3 (Figure S4). This indicates that flow velocity within the HZ also plays an important role in the dynamics of transport at watershed scales. Of the four experiments, the latter two (E3, E4) are closer to the baseline simulation and observations, suggesting the strong influences of hyporheic processes and streamflow on transport modeling.

At river network scale, our connectivity-based model reproduces the BTCs of the RWT tracer over an entire dry season in 2003 and sheds light on our understanding of how river network geometry affects transport dynamics. The residence time of the RWT in the streams is largely controlled by sediment sorption and the travel time distribution in the HZ before the RWT returns to the main channel. These multiscale dynamics becomes more complex in the context of river network under the effects of time delay and transformation. The long-term network-scale observations of RWT tracer over entire dry season provide a great opportunity to model these multiscale dynamics. In general, model

results show very good agreement between observed and modeled BTC across scales and most of the sites, demonstrating the ability of the graph model to properly capture the complex dynamics of solute transport on the stream network. The model developed above offers a new opportunity for solute transport modeling at watershed and larger scales.

Our simplified model has several limitations however, and here we discuss only the major ones. First, the model struggles to accurately capture the abrupt changes in the BTCs observed at upstream sites LTT-1 and LTT-2 immediately after the injection ceases. During this time frames, the transport dynamics near the injection site are influenced by a number of in-channel and HZ processes. To enhance the model performance, it would be necessary to use more robust optimization techniques such as the MCMC for parameter estimation. Second, the model tends to overestimate concentration at site LTT-4 toward the end of the simulation period. This could be attributed to the underestimation of streamflow by the EA-LSTM at nodes near this site during the dry season. Site LLT-4 is below the confluence with Cold Creek, where the baseflow contribution is approximate one order of magnitude greater than the rest of Lookout Creek watershed (Segura et al., 2019). Further research is warranted to incorporate more accurate representation of landforms and geology into the EA-LSTM to enhance the simulation of rainfall-runoff process during periods of low flow.

4. Summary and conclusions

An important challenge in modeling solute transport at watershed scales is to simultaneously represent the effects of large-scale stream networks and fine-scale gradients in geochemical conditions along diverse hydrologic pathways. In this paper, we present a machine-learning-assisted conceptual framework for modeling the long-term dynamics of solute transport at watershed scales. Our framework relies on performing a process-based scaling of network geometry to convert the network width function into a time response function where the process of interest is the transport of solute (e.g., RWT). Here the dynamics of solute in the stream network is modeled using an unsteady multiscale framework (ADELS) that includes and describes the HZ transport system in Lagrangian form as a subgrid model (Le et al., 2023). The framework is applied to the HJA experimental forest
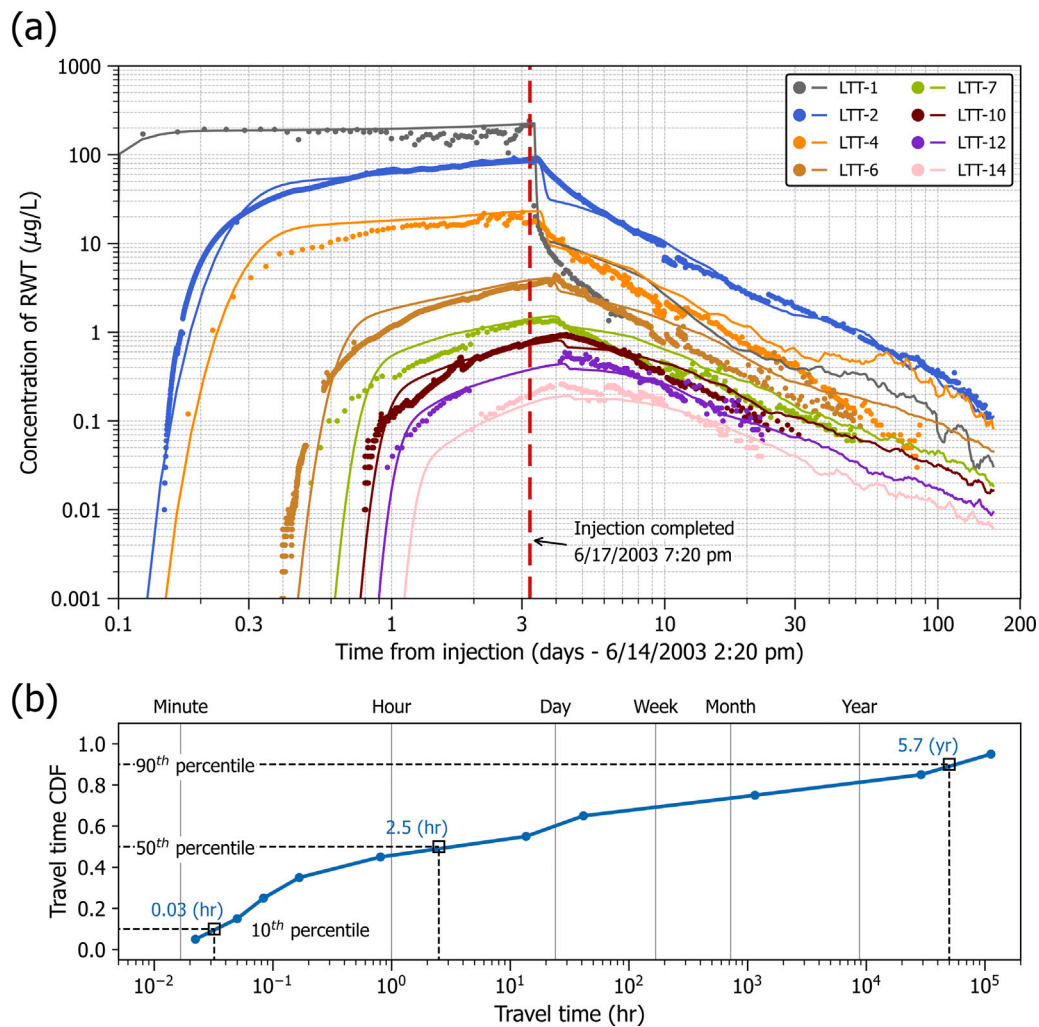
Fig. 9. (a) Comparison of modeled (solid lines) and observed (dots) breakthrough curves of RWT solute concentration for 8 monitoring sites during the longitudinal tracer test (LTT) in summer 2003. Horizontal and vertical axes are in log scale. The vertical red dashed line indicates the time injection ended on June 17, 2003. (b) Cumulative distribution function of travel time in the hyporheic zone (HZ). The travel time is assumed spatially homogeneous over the entire river network. The annotation shows the travel time values corresponding to the 10th, 50th, and 90th percentiles. (For interpretation of the references to color in this figure legend, the reader is referred to the web version of this article.)

using months-long tracer tests during the dry season in 2003 to help in understanding the multiscale dynamics and control of watershed characteristics on solute transport.

It is shown that the stream network geometry and transport dynamics in the HJA combine to produce a complex response function of RWT along the main channel of the Lookout Creek watershed. The multiscale model is able to reproduce the power-law scaling behaviors of the BTCs indicative of a very wide range of residence time distribution of solutes in stream network systems. Our findings suggest the important roles of HZ in controlling the time response function of solute transport at large spatial scales (e.g., watershed). For RWT, the response function is also known to be affected by the process of sorption to sediment (Runkel, 2015; Keefe et al., 2004) as implemented in Eq. (B.1). In this study, the streamflow along the river network is reconstructed using rainfall-runoff modeling based on the EA-LSTM neural network (Kratzert et al., 2019b). The EA-LSTM model is able to capture, spatially and temporally, the magnitudes of streamflow over the entire Lookout Creek watershed from daily rainfall inputs which is critical to simulate accurately solute transport in stream channels during dry (low flow) season. Nevertheless, this approach requires long-term and extensive observations of streamflow at multiple sub-basins in the study area to be able to well train the deep learning neural network. A direction for future work is to integrate the multiscale river corridor into physically-based models, which will enable the representation of

land surface processes, biogeochemical effects of long range hydrologic pathways and regional-scale groundwater flows.

CRediT authorship contribution statement

Phong V.V. Le: Writing – original draft, Visualization, Software, Methodology, Formal analysis, Data curation, Conceptualization. **Saubhagya S. Rathore:** Writing – review & editing, Visualization, Software, Methodology. **Ethan T. Coon:** Writing – review & editing, Software, Methodology. **Adam Ward:** Writing – review & editing, Data curation. **Roy Haggerty:** Writing – review & editing, Data curation. **Scott L. Painter:** Writing – review & editing, Project administration, Methodology, Funding acquisition, Data curation, Conceptualization.

Declaration of competing interest

The authors declare that they have no known competing financial interests or personal relationships that could have appeared to influence the work reported in this paper.

Data availability

Data will be made available on request.

Acknowledgments

Appendix A. EA-LSTM neural network

The forward pass of the EA-LSTM is described by the following equations (Kratzert et al., 2019b):

$$i = \sigma(W_i x_s + b_i) \tag{A.1a}$$

$$f(t) = \sigma(W_f x_d(t) + U_f h(t-1) + b_f) \tag{A.1b}$$

$$g(t) = \tanh(W_g x_d(t) + U_g h(t-1) + b_g) \tag{A.1c}$$

$$o(t) = \sigma(W_o x_d(t) + U_o h(t-1) + b_o) \tag{A.1d}$$

$$c(t) = f(t) \odot c(t-1) + i \odot g(t) \tag{A.1e}$$

$$h(t) = o(t) \odot \tanh(c(t)) \tag{A.1f}$$

where t represents time [T]; i is an input gate which does not change over time and only processes the static inputs x_s (e.g., basin attributes); $f(t)$ and $o(t)$ are the time-dependent forget and output gates, respectively; $x_d(t)$ are the dynamics inputs at time t (e.g., meteorological forcings); $h(t)$ and $c(t)$ represents hidden and cell states; W, U, and b are learnable parameters for each gate, σ is the sigmoid function, $\tanh$ is the hyperbolic tangent function, and $\odot$ represents the element-wise multiplication. In the EA-LSTM network, the static input x_s and dynamic input $x_d(t)$ are processed separately for different tasks. Through input gate i, the static features control parts of the LSTM are activated for any individual catchment, while the dynamic and recurrent inputs control information written into the cell g for memory, forget gate $f(t)$, and output gate $o(t)$ at time t.

When calculate over data from multiple sub-basins, an objective function that does not depend on the basin-specific outputs is required. Here we use the basin-averaged Nash–SutcliffeEfficiency (NSE) index (Kratzert et al., 2019b) as a loss function for training the EA-LSTM model:

$$NSE = \frac{1}{B} \sum_{b=1}^{B} \sum_{m=1}^{M} \frac{(\hat{y}_m - y_m)^2}{(s_b + \epsilon)^2} \tag{A.2}$$

where B is the number of sub-basins, M is the number of samples (e.g., days) per basin, $\hat{y}_m$ is the prediction of streamflow of sample m ($1 \leq m \leq M$), y_m is the observation of streamflow of sample m, s_b is the standard deviation of streamflow in the basin b calculated from the training period, and $\epsilon = 0.1$ is a constant term added to the denominator so that the loss function does not explode for sub-basins with very low streamflow variance (Kratzert et al., 2019b).

Appendix B. ADELS framework

For tracers on a single reach under unsteady flow, ADELS model is expressed mathematically as (Le et al., 2023):

$$A\frac{\partial C}{\partial t} + \frac{\partial (QC)}{\partial x} - \frac{\partial}{\partial x}\left(AD\frac{\partial C}{\partial x}\right) = -\alpha AC + \alpha A \int_0^\infty C_{hz}(x,t,\mathcal{T})\phi(\mathcal{T})d\mathcal{T} \tag{B.1a}$$

$$\left(1 + \frac{\rho_b K_d}{\theta}\right)\frac{\partial C_{hz}}{\partial t} + v\frac{\partial C_{hz}}{\partial \tau} = 0 \tag{B.1b}$$

$$C_{hz}(x,t,0) = C(x,t) \tag{B.1c}$$

where x denotes the distance along the channel [L], t represents time [T], $C(x,t)$ is the concentration in the channel [ML^{-3}], $D(x,t)$ is longitudinal dispersion coefficient [$L^2 T^{-1}$], $Q(x,t)$ is channel flow [$L^3 T^{-1}$], $A(x,t)$ is the channel wet cross-section area [L^2], $K_d(x)$ is sorption coefficient of solute in the HZ [$L^3 M^{-1}$], ρ_b is bulk density [ML^{-3}], $C_{hz}(x,t,\tau)$ represents concentration in the HZ [ML^{-3}], τ is hyporheic age or the time elapsed by a tracer since it starts moving on a hyporheic streamline [T], $\phi(\mathcal{T})$ is the probability density function (pdf) of travel time $\mathcal{T}$ in the HZ, and $\alpha(x,t)$ is the hyporheic exchange rate [T^{-1}] calculated as:

$$\alpha(x,t) = \alpha_0(x)f_Q(x,t)^{\beta_\alpha(x)} \tag{B.2}$$

where $\alpha_0(x)$ represents the pseudo-mean rate of water turnover through the HZ [T^{-1}], $\beta_\alpha(x)$ is the scaling exponent of hyporheic exchange due to variation of head boundary on the stream bed, and $f_Q(x,t)$ [–] is the flow-factor (Selroos et al., 2013; Sanz-Prat et al., 2016) representing the fluctuation of streamflow around the long-term mean:

$$f_Q(x,t) = \frac{Q(x,t)}{\langle Q(x,t)\rangle_t} \tag{B.3}$$

The longitudinal dispersion coefficient is calculated as follows (Fischer, 1975; Antonopoulos et al., 2015):

$$D(x,t) = D_0(x) \times f_Q(x,t)^{\beta_D(x)} \tag{B.4}$$

where $D_0(x)$ [$L^2 T^{-1}$] is the mean longitudinal dispersion coefficient and $\beta_D(x)$ [–] is the scaling factor representing the fluctuation of longitudinal dispersion coefficient around the mean value. In Eq. Eq. (B.1b), the usual Lagrangian form of the solute transport equation is modified to include a pseudo-velocity $v(x,t)$ to represent fluctuations of the Darcy velocity around steady-state conditions as in Selroos et al. (2013) and Sanz-Prat et al. (2016). In the current context, we relate this flow factor to channel discharge

$$v(x,t) = f_Q(x,t)^{\beta_v} \tag{B.5}$$

where the parameter β_v represents the scaling exponent [–] for velocity changes in the HZ due to the variation of head boundary on the stream bed (Le et al., 2023). Finally, $A(x,t) = w(x,t) \times d(x,t)$ where flow depth $d(x,t)$ [L] and width $w(x,t)$ [L] are obtained using the hydraulic geometry scaling relations in the form of power functions of $Q(x,t)$ described by Leopold and Maddock (1953) as follows:

$$d(x,t) = b_d Q(x,t)^{a_d} \tag{B.6a}$$

$$w(x,t) = b_w Q(x,t)^{a_w} \tag{B.6b}$$

where a_d, b_d, a_w, and b_w are empirical regression parameters.

Appendix C. Supplementary data

Supplementary material related to this article can be found online at https://doi.org/10.1016/j.jhydrol.2024.131562.

References

Andre, B., Molins, S., Johnson, J., Steefel, C., 2013. Alquimia. Comput. Softw. http://dx.doi.org/10.11578/dc.20210416.49, Retrieved from https://doi.org/10.11578/dc.20210416.49.

Antonopoulos, V.Z., Georgiou, P.E., Antonopoulos, Z.V., 2015. Dispersion coefficient prediction using Empirical Models and ANNs. Environ. Process. 2 (2), 379–394. http://dx.doi.org/10.1007/s40710-015-0074-6.

Azizian, M., Boano, F., Cook, P.L.M., Detwiler, R.L., Rippy, M.A., Grant, S.B., 2017. Ambient groundwater flow diminishes nitrate processing in the hyporheic zone of streams. Water Resour. Res. 53 (5), 3941–3967. http://dx.doi.org/10.1002/2016WR020048.

Azizian, M., Grant, S.B., Kessler, A.J., Cook, P.L.M., Rippy, M.A., Stewardson, M.J., 2015. Bedforms as Biocatalytic Filters: A pumping and streamline segregation model for nitrate removal in permeable sediments. Environ. Sci. Technol. 49 (18), 10993–11002. http://dx.doi.org/10.1021/acs.est.5b01941.

Battin, T.J., Kaplan, L.A., Findlay, S., Hopkinson, C.S., Marti, E., Packman, A.I., Newbold, J.D., Sabater, F., 2008. Biophysical controls on organic carbon fluxes in fluvial networks. Nat. Geosci. 1 (2), 95–100. http://dx.doi.org/10.1038/ngeo101.

Bencala, K.E., Gooseff, M.N., Kimball, B.A., 2011. Rethinking hyporheic flow and transient storage to advance understanding of stream-catchment connections. Water Resour. Res. 47 (3), http://dx.doi.org/10.1029/2010WR010066.

Bencala, K.E., Walters, R.A., 1983. Simulation of solute transport in a mountain pool-and-riffle stream: A transient storage model. Water Resour. Res. 19 (3), 718–724. http://dx.doi.org/10.1029/WR019i003p00718.

Bertuzzo, E., Helton, A.M., Hall, R.O., Battin, T.J., 2017. Scaling of dissolved organic carbon removal in river networks. Adv. Water Resour. 110, 136–146. http://dx.doi.org/10.1016/j.advwatres.2017.10.009.

Boano, F., Demaria, A., Revelli, R., Ridolfi, L., 2010. Biogeochemical zonation due to intrameander hyporheic flow. Water Resour. Res. 46 (2), http://dx.doi.org/10.1029/2008WR007583.

Boano, F., Harvey, J.W., Marion, A., Packman, A.I., Revelli, R., Ridolfi, L., Wörman, A., 2014. Hyporheic flow and transport processes: Mechanisms, models, and biogeochemical implications. Rev. Geophys. 52 (4), 603–679. http://dx.doi.org/10.1002/2012RG000417.

Boano, F., Packman, A.I., Cortis, A., Revelli, R., Ridolfi, L., 2007. A continuous time random walk approach to the stream transport of solutes. Water Resour. Res. 43 (10), http://dx.doi.org/10.1029/2007WR006062.

Boano, F., Revelli, R., Ridolfi, L., 2009. Quantifying the impact of groundwater discharge on the surface–subsurface exchange. Hydrol. Process. 23 (15), 2108–2116. http://dx.doi.org/10.1002/hyp.7278.

Boulton, A.J., Findlay, S., Marmonier, P., Stanley, E.H., Valett, H.M., 1998. The functional significance of the hyporheic zone in streams and rivers. Annu. Rev. Ecol. Syst. 29 (1), 59–81. http://dx.doi.org/10.1146/annurev.ecolsys.29.1.59.

Cardenas, M.B., 2009. Stream-aquifer interactions and hyporheic exchange in gaining and losing sinuous streams. Water Resour. Res. 45 (6), http://dx.doi.org/10.1029/2008WR007651.

Cardenas, M.B., 2015. Hyporheic zone hydrologic science: A historical account of its emergence and a prospectus. Water Resour. Res. 51 (5), 3601–3616. http://dx.doi.org/10.1002/2015WR017028.

Conant, B., Cherry, J.A., Gillham, R.W., 2004. A PCE groundwater plume discharging to a river: influence of the streambed and near-river zone on contaminant distributions. J. Contam. Hydrol. 73 (1), 249–279. http://dx.doi.org/10.1016/j.jconhyd.2004.04.001.

Coon, E., Svyatsky, D., Jan, A., Kikinzon, E., Berndt, M., Atchley, A., Harp, D., Manzini, G., Shelef, E., Lipnikov, K., Garimella, R., Xu, C., Moulton, D., Karra, S., Painter, S., Jafarov, E., Molins, S., 2019. Advanced terrestrial simulator. Comput. Softw. http://dx.doi.org/10.11578/dc.20190911.1, Retrieved from https://doi.org/10.11578/dc.20190911.1.

Courant, R., Friedrichs, K., Lewy, H., 1967. On the partial difference equations of mathematical physics. IBM J. Res. Dev. 11 (2), 215–234. http://dx.doi.org/10.1147/rd.112.0215.

Cvetkovic, V., Dagan, G., 1994. Transport of kinetically sorbing solute by steady random velocity in heterogeneous porous formations. J. Fluid Mech. 265, 189–215. http://dx.doi.org/10.1017/S0022112094000807.

Czuba, J.A., Foufoula-Georgiou, E., 2014. A network-based framework for identifying potential synchronizations and amplifications of sediment delivery in river basins. Water Resour. Res. 50 (5), 3826–3851. http://dx.doi.org/10.1002/2013WR014227.

Czuba, J.A., Hansen, A.T., Foufoula-Georgiou, E., Finlay, J.C., 2018. Contextualizing wetlands within a river network to assess nitrate removal and inform watershed management. Water Resour. Res. 54 (2), 1312–1337. http://dx.doi.org/10.1002/2017WR021859.

Dagan, G., Cvetkovic, V., 1993. Spatial moments of a kinetically sorbing solute plume in a heterogeneous aquifer. Water Resour. Res. 29 (12), 4053–4061. http://dx.doi.org/10.1029/93WR02299.

Dwivedi, D., Steefel, C.I., Arora, B., Newcomer, M., Moulton, J.D., Dafflon, B., Faybishenko, B., Fox, P., Nico, P., Spycher, N., Carroll, R., Williams, K.H., 2018. Geochemical exports to river from the intrameander hyporheic zone under transient hydrologic conditions: East River Mountainous Watershed, Colorado. Water Resour. Res. 54 (10), 8456–8477. http://dx.doi.org/10.1029/2018WR023377.

Fang, Y., Chen, X., Gomez Velez, J., Zhang, X., Duan, Z., Hammond, G.E., Goldman, A.E., Garayburu-Caruso, V.A., Graham, E.B., 2020. A multirate mass transfer model to represent the interaction of multicomponent biogeochemical processes between surface water and hyporheic zones (swat-mrmt-r 1.0). Geoscientific Model Development 13 (8), 3553–3569. http://dx.doi.org/10.5194/gmd-13-3553-2020, https://gmd.copernicus.org/articles/13/3553/2020/.

Fischer, H.B., 1975. Simple method for predicting dispersion in streams. J. Environ. Eng. Div. 101 (3), 453–455. http://dx.doi.org/10.1061/JEEGAV.0000360.

Frame, J.M., Kratzert, F., Klotz, D., Gauch, M., Shalev, G., Gilon, O., Qualls, L.M., Gupta, H.V., Nearing, G.S., 2022. Deep learning rainfall–runoff predictions of extreme events. Hydrol. Earth Syst. Sci. 26 (13), 3377–3392. http://dx.doi.org/10.5194/hess-26-3377-2022.

Fuller, C.C., Harvey, J.W., 2000. Reactive uptake of trace metals in the hyporheic zone of a mining-contaminated stream, Pinal Creek, Arizona. Environ. Sci. Technol. 34 (7), 1150–1155. http://dx.doi.org/10.1021/es990714d.

Gomez, J.D., Wilson, J.L., Cardenas, M.B., 2012. Residence time distributions in sinuosity-driven hyporheic zones and their biogeochemical effects. Water Resour. Res. 48 (9), http://dx.doi.org/10.1029/2012WR012180.

Gomez-Velez, J.D., Krause, S., Wilson, J.L., 2014. Effect of low-permeability layers on spatial patterns of hyporheic exchange and groundwater upwelling. Water Resour. Res. 50 (6), 5196–5215. http://dx.doi.org/10.1002/2013WR015054.

Gooseff, M.N., Bencala, K.E., Wondzell, S.M., 2008. Solute transport along stream and river networks. In: River Confluences, Tributaries and the Fluvial Network. John Wiley & Sons, Ltd, pp. 395–417. http://dx.doi.org/10.1002/9780470760383.ch18.

Gooseff, M.N., LaNier, J., Haggerty, R., Kokkeler, K., 2005. Determining in-channel (dead zone) transient storage by comparing solute transport in a bedrock channel–alluvial channel sequence, Oregon. Water Resour. Res. 41 (6), http://dx.doi.org/10.1029/2004WR003513.

Gooseff, M.N., Wondzell, S.M., Haggerty, R., Anderson, J., 2003. Comparing transient storage modeling and residence time distribution (RTD) analysis in geomorphically varied reaches in the Lookout Creek basin, Oregon, USA. Adv. Water Resour. 26 (9), 925–937. http://dx.doi.org/10.1016/S0309-1708(03)00105-2, Modeling Hyporheic Zone Processes.

Gravelius, H., 1914. Flusskunde. G.J. göschen.

Hack, J.T., 1957. Studies of Longitudinal Stream Profiles in Virginia and Maryland, Tech. Rep., Report, - ed. http://dx.doi.org/10.3133/pp294B.

Haggerty, R., Ninnemann, J.J., 2013. A Study of Hyporheic Characteristics Along a Longitudinal Profile of Lookout Creek, Oregon, 2003. Long-Term Ecological Research. Forest Science Data Bank, Corvallis, OR, Retrieved from https://doi.org/10.6073/pasta/2c149c55bcc729b9cbc7f17fe286ad50. (Accessed 02 June 2023).

Haggerty, R., Wondzell, S.M., Johnson, M.A., 2002. Power-law residence time distribution in the hyporheic zone of a 2nd-order mountain stream. Geophys. Res. Lett. 29 (13), 18–1–18–4. http://dx.doi.org/10.1029/2002GL014743.

Hammond, G.E., Lichtner, P.C., Mills, R.T., 2014. Evaluating the performance of parallel subsurface simulators: An illustrative example with PFLOTRAN. Water Resour. Res. 50 (1), 208–228. http://dx.doi.org/10.1002/2012WR013483.

Harvey, J.W., Fuller, C.C., 1998. Effect of enhanced manganese oxidation in the hyporheic zone on basin-scale geochemical mass balance. Water Resour. Res. 34 (4), 623–636. http://dx.doi.org/10.1029/97WR03606.

Harvey, J.W., Wagner, B.J., Bencala, K.E., 1996. Evaluating the reliability of the stream tracer approach to characterize stream-subsurface water exchange. Water Resour. Res. 32 (8), 2441–2451. http://dx.doi.org/10.1029/96WR01268.

Hedin, L.O., von Fischer, J.C., Ostrom, N.E., Kennedy, B.P., Brown, M.G., Robertson, G.P., 1998. Thermodynamic constraints on nitrogen transformations and other biogeochemical processes at soil-stream interfaces. Ecology 79 (2), 684–703.

Helton, A.M., Poole, G.C., Meyer, J.L., Wollheim, W.M., Peterson, B.J., Mulholland, P.J., Bernhardt, E.S., Stanford, J.A., Arango, C., Ashkenas, L.R., Cooper, L.W., Dodds, W.K., Gregory, S.V., Hall Jr., R.O., Hamilton, S.K., Johnson, S.L., McDowell, W.H., Potter, J.D., Tank, J.L., Thomas, S.M., Valett, H.M., Webster, J.R., Zeglin, L., 2011. Thinking outside the channel: modeling nitrogen cycling in networked river ecosystems. Front. Ecol. Environ. 9 (4), 229–238. http://dx.doi.org/10.1890/080211.

Hochreiter, S., Schmidhuber, J., 1997. Long short-term memory. Neural Comput. 9 (8), 1735–1780. http://dx.doi.org/10.1162/neco.1997.9.8.1735.

Hoedt, P.-J., Kratzert, F., Klotz, D., Halmich, C., Holzleitner, M., Nearing, G.S., Hochreiter, S., Klambauer, G., 2021. MC-LSTM: Mass-conserving LSTM. In: Meila, M., Zhang, T. (Eds.), Proceedings of the 38th International Conference on Machine Learning. In: Proceedings of Machine Learning Research, Vol. 139, PMLR, pp. 4275–4286.

Jan, A., Coon, E.T., Painter, S.L., 2021. Toward more mechanistic representations of biogeochemical processes in river networks: Implementation and demonstration of a multiscale model. Environ. Model. Softw. 145, 105166. http://dx.doi.org/10.1016/j.envsoft.2021.105166.

Johnson, S.L., Henshaw, D., Downing, G., Wondzell, S., Schulze, M., Kennedy, A., Cohn, G., Schmidt, S.A., Jones, J.A., 2021. Long-term hydrology and aquatic biogeochemistry data from H. J. Andrews Experimental Forest, Cascade Mountains, Oregon. Hydrol. Process. 35 (5), e14187. http://dx.doi.org/10.1002/hyp.14187.

Keefe, S.H., Barber, L.B., Runkel, R.L., Ryan, J.N., McKnight, D.M., Wass, R.D., 2004. Conservative and reactive solute transport in constructed wetlands. Water Resour. Res. 40 (1), http://dx.doi.org/10.1029/2003WR002130.

Knapp, J.L.A., Cirpka, O.A., 2017. Determination of hyporheic travel time distributions and other parameters from concurrent conservative and reactive tracer tests by local-in-global optimization. Water Resour. Res. 53 (6), 4984–5001. http://dx.doi.org/10.1002/2017WR020734, Retrieved from https://agupubs.onlinelibrary.wiley.com/doi/abs/10.1002/2017WR020734.

Kratzert, F., Klotz, D., Herrnegger, M., Sampson, A.K., Hochreiter, S., Nearing, G.S., 2019a. Toward improved predictions in ungauged basins: Exploiting the power of machine learning. Water Resour. Res. 55 (12), 11344–11354. http://dx.doi.org/10.1029/2019WR026065.

Kratzert, F., Klotz, D., Shalev, G., Klambauer, G., Hochreiter, S., Nearing, G., 2019b. Towards learning universal, regional, and local hydrological behaviors via machine learning applied to large-sample datasets. Hydrol. Earth Syst. Sci. 23 (12), 5089–5110. http://dx.doi.org/10.5194/hess-23-5089-2019.

Le, P.V., Rathore, S.S., Painter, S.L., 2023. A multiscale model for solute transport in stream corridors with unsteady flow. J. Hydrol. 129670. http://dx.doi.org/10.1016/j.jhydrol.2023.129670.

Leopold, L.B., Maddock, Jr., T., 1953. The Hydraulic Geometry of Stream Channels and Some Physiographic Implications. Tech. Rep., Report, Washington, D.C., p. 64. http://dx.doi.org/10.3133/pp252.

Liao, Z., Cirpka, O.A., 2011. Shape-free inference of hyporheic traveltime distributions from synthetic conservative and "smart" tracer tests in streams. Water Resour. Res. 47 (7), http://dx.doi.org/10.1029/2010WR009927.

Liao, Z., Lemke, D., Osenbrück, K., Cirpka, O.A., 2013. Modeling and inverting reactive stream tracers undergoing two-site sorption and decay in the hyporheic zone. Water Resour. Res. 49 (6), 3406–3422. http://dx.doi.org/10.1002/wrcr.20276.

Marzadri, A., Tonina, D., Bellin, A., 2011. A semianalytical three-dimensional process-based model for hyporheic nitrogen dynamics in gravel bed rivers. Water Resour. Res. 47 (11), http://dx.doi.org/10.1029/2011WR010583.

Marzadri, A., Tonina, D., Bellin, A., 2012. Morphodynamic controls on redox conditions and on nitrogen dynamics within the hyporheic zone: Application to gravel bed rivers with alternate-bar morphology. J. Geophys. Res.: Biogeosci. 117 (G3), http://dx.doi.org/10.1029/2012JG001966.

Marzadri, A., Tonina, D., Bellin, A., 2013. Effects of stream morphodynamics on hyporheic zone thermal regime. Water Resour. Res. 49 (4), 2287–2302.

Molins, S., Svyatsky, D., Xu, Z., Coon, E.T., Moulton, J.D., 2022. A multicomponent reactive transport model for integrated surface-subsurface hydrology problems. Water Resour. Res. 58 (8), e2022WR032074. http://dx.doi.org/10.1029/2022WR032074.

Montgomery, D.R., Dietrich, W.E., 1992. Channel initiation and the problem of landscape scale. Science 255 (5046), 826–830. http://dx.doi.org/10.1126/science.255.5046.826.

Mulholland, P.J., Helton, A.M., Poole, G.C., Hall, R.O., Hamilton, S.K., Peterson, B.J., Tank, J.L., Ashkenas, L.R., Cooper, L.W., Dahm, C.N., Dodds, W.K., Findlay, S.E.G., Gregory, S.V., Grimm, N.B., Johnson, S.L., McDowell, W.H., Meyer, J.L., Valett, H.M., Webster, J.R., Arango, C.P., Beaulieu, J.J., Bernot, M.J., Burgin, A.J., Crenshaw, C.L., Johnson, L.T., Niederlehner, B.R., O'Brien, J.M., Potter, J.D., Sheibley, R.W., Sobota, D.J., Thomas, S.M., 2008. Stream denitrification across biomes and its response to anthropogenic nitrate loading. Nature 452 (7184), 202–205. http://dx.doi.org/10.1038/nature06686.

Nash, J., Sutcliffe, J., 1970. River flow forecasting through conceptual models part I — A discussion of principles. J. Hydrol. 10 (3), 282–290. http://dx.doi.org/10.1016/0022-1694(70)90255-6.

Ninnemann, J.J., 2005. A Study of Hyporheic Characteristics Along a Longitudinal Profile of Lookout Creek, Oregon (Master's thesis). Oregon State University, Available at https://ir.library.oregonstate.edu/concern/graduate_thesis_or_dissertations/ng451m513, Unpublished.

Packman, A.I., Brooks, N.H., 2001. Hyporheic exchange of solutes and colloids with moving bed forms. Water Resour. Res. 37 (10), 2591–2605. http://dx.doi.org/10.1029/2001WR000477.

Painter, S.L., 2018. Multiscale framework for modeling multicomponent reactive transport in stream corridors. Water Resour. Res. 54 (10), 7216–7230. http://dx.doi.org/10.1029/2018WR022831, Retrieved from https://agupubs.onlinelibrary.wiley.com/doi/abs/10.1029/2018WR022831.

Palumbo-Roe, B., Wragg, J., Banks, V.J., 2012. Lead mobilisation in the hyporheic zone and river bank sediments of a contaminated stream: contribution to diffuse pollution. J. Soils Sediments 12 (10), 1633–1640. http://dx.doi.org/10.1007/s11368-012-0552-7.

Rathore, S.S., Jan, A., Coon, E.T., Painter, S.L., 2021. On the reliability of parameter inferences in a multiscale model for transport in stream corridors. Water Resour. Res. 57 (5), e2020WR028908. http://dx.doi.org/10.1029/2020WR028908, Retrieved from https://agupubs.onlinelibrary.wiley.com/doi/abs/10.1029/2020WR028908.

Rathore, S.S., Ward, A.S., Painter, S.L., 2023. Numerical evaluation of photosensitive tracers as a strategy for separating surface and subsurface transient storage in streams. J. Hydrol. 624, 129931. http://dx.doi.org/10.1016/j.jhydrol.2023.129931.

Revelli, R., Boano, F., Camporeale, C., Ridolfi, L., 2008. Intra-meander hyporheic flow in alluvial rivers. Water Resour. Res. 44 (12), http://dx.doi.org/10.1029/2008WR007081.

Riml, J., Wörman, A., 2011. Response functions for in-stream solute transport in river networks. Water Resour. Res. 47 (6), http://dx.doi.org/10.1029/2010WR009412.

Rodriguez, N.B., McGuire, K.J., Klaus, J., 2018. Time-varying storage–water age relationships in a catchment with a Mediterranean Climate. Water Resour. Res. 54 (6), 3988–4008. http://dx.doi.org/10.1029/2017WR021964.

Rodriguez-Iturbe, I., Muneepeerakul, R., Bertuzzo, E., Levin, S.A., Rinaldo, A., 2009. River networks as ecological corridors: A complex systems perspective for integrating hydrologic, geomorphologic, and ecologic dynamics. Water Resour. Res. 45 (1), http://dx.doi.org/10.1029/2008WR007124.

Runkel, R.L., 1998. One-Dimensional Transport with Inflow and Storage (OTIS): A Solute Transport Model for Streams and Rivers, Tech. Rep. Report, - ed. http://dx.doi.org/10.3133/wri984018.

Runkel, R.L., 2007. Toward a transport-based analysis of nutrient spiraling and uptake in streams. Limnol. Oceanogr.: Methods 5 (1), 50–62. http://dx.doi.org/10.4319/lom.2007.5.50.

Runkel, R.L., 2015. On the use of rhodamine WT for the characterization of stream hydrodynamics and transient storage. Water Resour. Res. 51 (8), 6125–6142. http://dx.doi.org/10.1002/2015WR017201.

Runkel, R.L., Chapra, S.C., 1993. An efficient numerical solution of the transient storage equations for solute transport in small streams. Water Resour. Res. 29 (1), 211–215. http://dx.doi.org/10.1029/92WR02217.

Sanz-Prat, A., Lu, C., Finkel, M., Cirpka, O.A., 2015. On the validity of travel-time based nonlinear bioreactive transport models in steady-state flow. J. Contam. Hydrol. 175–176, 26–43. http://dx.doi.org/10.1016/j.jconhyd.2015.02.003.

Sanz-Prat, A., Lu, C., Finkel, M., Cirpka, O.A., 2016. Using travel times to simulate multi-dimensional bioreactive transport in time-periodic flows. J. Contam. Hydrol. 187, 1–17. http://dx.doi.org/10.1016/j.jconhyd.2016.01.005.

Schaper, J.L., Posselt, M., McCallum, J.L., Banks, E.W., Hoehne, A., Meinikmann, K., Shanafield, M.A., Batelaan, O., Lewandowski, J., 2018. Hyporheic exchange controls fate of trace organic compounds in an urban stream. Environ. Sci. Technol. 52 (21), 12285–12294. http://dx.doi.org/10.1021/acs.est.8b03117.

Segura, C., Noone, D., Warren, D., Jones, J.A., Tenny, J., Ganio, L.M., 2019. Climate, landforms, and geology affect baseflow sources in a Mountain catchment. Water Resour. Res. 55 (7), 5238–5254. http://dx.doi.org/10.1029/2018WR023551.

Selroos, J.-O., Cheng, H., Painter, S., Vidstrand, P., 2013. Radionuclide transport during glacial cycles: Comparison of two approaches for representing flow transients. Phys. Chem. Earth A/B/C 64, 32–45. http://dx.doi.org/10.1016/j.pce.2012.10.003.

Swanson, F.J., 1975. Geology and Geomorphology of the HJ Andrews Experimental Forest, Western Cascades, Oregon, vol. 188–204, Pacific Northwest Forest and Range Experiment Station, Forest Service, US Department of Agriculture.

Swanson, F.J., 2005. Upper Blue River Geology Clipped to the Andrews Experimental Forest. Long-Term Ecological Research. Forest Science Data Bank, Corvallis, OR, Retrieved from https://doi.org/10.6073/pasta/1c428e8798a2f3975f202636d3ad6139. (Accessed: 12 May 2024).

Tonina, D., Buffington, J.M., 2011. Effects of stream discharge, alluvial depth and bar amplitude on hyporheic flow in pool-riffle channels. Water Resour. Res. 47 (8), http://dx.doi.org/10.1029/2010WR009140.

Voltz, T., Gooseff, M., Ward, A.S., Singha, K., Fitzgerald, M., Wagener, T., 2013. Riparian hydraulic gradient and stream-groundwater exchange dynamics in steep headwater valleys. J. Geophys. Res.: Earth Surf. 118 (2), 953–969. http://dx.doi.org/10.1002/jgrf.20074.

Ward, A.S., 2016. The evolution and state of interdisciplinary hyporheic research. WIREs Water 3 (1), 83–103. http://dx.doi.org/10.1002/wat2.1120.

Whitehead, P., Wilson, E., Butterfield, D., 1998. A semi-distributed Integrated Nitrogen model for multiple source assessment in Catchments (INCA): Part I — model structure and process equations. Sci. Total Environ. 210–211, 547–558. http://dx.doi.org/10.1016/S0048-9697(98)00037-0.

Wörman, A., Packman, A.I., Johansson, H., Jonsson, K., 2002. Effect of flow-induced exchange in hyporheic zones on longitudinal transport of solutes in streams and rivers. Water Resour. Res. 38 (1), http://dx.doi.org/10.1029/2001WR000769, 2–1–2–15.

Ye, S., Covino, T.P., Sivapalan, M., Basu, N.B., Li, H.-Y., Wang, S.-W., 2012. Dissolved nutrient retention dynamics in river networks: A modeling investigation of transient flows and scale effects. Water Resour. Res. 48 (6), http://dx.doi.org/10.1029/2011WR010508.

Zarnetske, J.P., Haggerty, R., Wondzell, S.M., Baker, M.A., 2011. Dynamics of nitrate production and removal as a function of residence time in the hyporheic zone. J. Geophys. Res.: Biogeosci. 116 (G1), http://dx.doi.org/10.1029/2010JG001356.